PCCP

PAPER

View Article Online
View Journal | View Issue

Cite this: *Phys. Chem. Chem. Phys.*, 2019, **21**, 20720

The use of ion-selective membranes to study cation transport in hybrid organic–inorganic perovskites†

Emily C. Smith, Christie L. C. Ellis, Hamza Javaid, Blaise G. Arden and D. Venkataraman *

Received 10th July 2019,
Accepted 26th August 2019

DOI: 10.1039/c9cp03891d

rsc.li/pccp

Using a methylammonium selective membrane in conjunction with electrochemical impedance spectroscopy, we measured ion migration in methylammonium lead triiodide ($MAPbI_3$) with a millisecond (ms) time constant under illumination. These values were consistent with the reported values of ionic conduction in thin-film perovskite solar cells. We monitored an electrochemical impedance response arising from ionic conductivity through $MAPbI_3$ and a methylammonium selective layer. We could fit this complex impedance response to an intuitive circuit model, which revealed an ionic species moving on a ms time scale. Electrospray ionization mass spectrometry (ESI-MS) revealed direct chemical evidence of methylammonium diffusion into the ion-selective layer. We found no experimental evidence indicating the mobility of lead ions or protons, suggesting that the mobile species observed under illumination is likely methylammonium.

A. Introduction

Ion transport, a central feature of hybrid organic–inorganic perovskite (HOIP) photovoltaics, affects many HOIP properties such as device stability, power conversion efficiencies (PCEs), and hysteresis in current density (J)–voltage (V) curves.[1–5] Despite the importance of mobile ions in HOIPs, the chemical identity of the mobile ions is still under debate. In HOIPs, it is likely that more than one mobile ion is responsible for the experimental observations of ion transport.[6–8] In the most commonly studied HOIP, namely, $(CH_3NH_3)PbI_3$, there are four possible mobile ions: H^+, $CH_3NH_3^+$ (MA^+), Pb^{2+} and I^-.[6] Moreover, light and electrical bias can and do influence ion transport, but their impact on each ion may differ. With multiple possibilities for mobile ions, the influence of solar cell operating conditions on ion mobility, and coupled charge transport, studying ion transport in these materials has not been straightforward. Methods such as pulse-field gradient NMR that can be used to identify the mobile ion chemically are difficult to run *in operando* (*i.e.*, under device-relevant conditions such as under light, heat and applied bias), whereas methods such as electrochemical impedance spectroscopy (EIS) that are convenient to study ion transport *in operando* lack chemical identity. These factors have led to diversity in opinions on the nature of the ion transport in HOIPs. For example, in thin-film HOIP photovoltaics with a p–i–n device architecture, we observed evidence of ion transport using EIS and calculated activation energy of 0.58 eV for the mobile ion in $MAPbI_3$, which we attributed to MA^+ migration. In a separate work, another group found the same activation energy barrier of 0.58 eV extrapolated from transient photovoltage decay measurements, but the value was attributed to I^- vacancy migration.[9] Understanding the nature and timescale of mobile ions is integral for fundamentally understanding the photovoltaic device performance and engineering new devices with improved stability. Additionally, a comprehensive knowledge of the nature of ion transport in a material will allow us to take advantage of the mixed ionic–electronic transport for various iontronic applications such as in electrochemical transistors and memristors for neuromorphic computing. Thus, it is imperative to determine ways to selectively study ion transport in these materials.

One technique that is widely used to probe ion transport in mixed ionic–electronic conductors is electrochemical impedance spectroscopy (EIS).[10–12] EIS allows the separation of the charge and mass transport processes that occur on different time scales, making it ideal for separating the electronic and ionic processes in HOIPs. From an EIS response, we can quantify kinetic parameters such as the diffusion constant and activation energy barriers of ion transport.[13] One important feature of EIS is that it can be used to study HOIP devices *in operando* to obtain critical information about device operational parameters on the electronic and ionic transport. A missing feature in the EIS response is the determination of ionic chemical identity. As a result, we can associate the features in EIS with an

Department of Chemistry, University of Massachusetts Amherst, Amherst Massachusetts 01003-9303, USA. E-mail: dv@chem.umass.edu

† Electronic supplementary information (ESI) available. See DOI: 10.1039/c9cp03891d

ionic process; however, we cannot conclusively relate these features to a particular ion. Thus, for HOIPs, where there is a possibility for more than one mobile ion, we raise the following question: which ion is responsible for the EIS features associated with ion transport? We hypothesized that placing an ion-selective membrane between the active layer and the electrode would allow us to associate the features in EIS with the selected ion. We reasoned that if we place an ion-selective membrane between the active layer and the electrode, then, the membrane will selectively allow one ion to reach the electrode, resulting in a primary EIS response from that ion. If we can attach chemical information to EIS data, which is the missing piece, we can selectively and quantitatively study each mobile ion in HOIPs under device-relevant conditions.

Herein, using a polymer ion-selective membrane (ISM) that was selective for methylammonium ions (MA^+), we studied the cationic transport in pristine methylammonium lead iodide ($MAPbI_3$) under illumination. We observed an EIS response consistent with ion transport through the material. The chemical characterization of the membrane using electrospray ionization mass spectrometry (ESI-MS) showed the presence of MA^+ in these membranes. We observed no evidence that the response arises from mobile Pb^{2+} or H^+. Furthermore, we observed negligible I^- incorporation into the membranes in the solid state. When we fitted the EIS response to an equivalent circuit model, we found that ion transport occurs in our device on the millisecond timescale, which is the same timescale commonly observed in EIS of thin-film photovoltaic devices; this was consistent with a mobile MA^+ ion.

B. Experimental

HOIP powder

$MAPbI_3$ powder was prepared as follows: a clean, dry 25 mL Erlenmeyer flask was charged with PbI_2 (552 mg, 1.19 mmol, Sigma Aldrich) and methylammonium iodide (202 mg, 1.27 mmol, GreatCell Solar) along with a stir bar. To the vial, γ-butyrolactone (4 mL, Sigma Aldrich) was added and the solution was ultrasonicated until all components were visibly solvated. The solution was stirred while dichloromethane (DCM, 8 mL, dried over magnesium sulfate anhydrous) was added dropwise. After the addition of DCM, stirring was stopped, and a black precipitate obtained was allowed to settle for 1 h before collection into two centrifuge tubes. The precipitate-containing solutions were centrifuged at 3500 rpm for 35 s or until the precipitate was fully sedimented. The remaining liquid was discarded, and the tubes containing the precipitate were filled with fresh DCM (10 mL). Each tube was ultrasonicated until the black powder was resuspended in the solution and centrifuged again at 3500 rpm for 35 s. The liquid was discarded. The powder was washed with DCM in this manner for further two times. The powder was air-dried for ~1 h and annealed at 100 °C for 1 h. The resulting $MAPbI_3$ powder (732 mg, 1.18 mmol, 99%) was stored in a vacuum oven overnight before further use. Powder X-ray diffraction (XRD) showed $MAPbI_3$ in the tetragonal phase and indicated no evidence of incomplete conversion from PbI_2 (Fig. S1, ESI†).

Ion-selective electrodes

ITO-coated glass substrates (1.5 cm × 1.5 cm, ~20 Ω sq^{-1}) were cleaned by the ultrasonication of the substrates submerged in soap and water, DI water, acetone, and isopropyl alcohol successively for 20 min each. Some ITO substrates were reused after testing to conserve resources. In the case of reuse, the substrates were first rinsed with tetrahydrofuran and then ultrasonicated with dichloromethane before cleaning using the above-mentioned procedure. The cleaned substrates were dried in an oven at 140 °C for at least 2 h before use. Methylammonium selective membranes were prepared as follows: to a clean, dry vial, polyvinylchloride (30 mg, 0.71 inherent viscosity, Acros Organics), dibenzo-18-crown-6 (2 mg, 5.5 μmol, Avacado Research Chemicals Ltd), bis(2-ethylhexyl)phthalate (DEHP) (110 μL, Sigma Aldrich) and tetrahydrofuran (1 mL, dried over 3 Å activated molecular sieves) were added. The components were ultrasonicated until the solids were fully dissolved. The solution was filtered through a 0.45 μm polytetrafluoroethylene (PTFE) filter (Restek). The membrane solution was drop-casted onto cleaned ITO substrates (100 μL) and then left to dry overnight before use.

HOIP pellets

Pellets of $MAPbI_3$ were prepared as follows: the $MAPbI_3$ powder was ground finely in a mortar and pestle lined with a clean weighing paper. Pellets were hand-pressed using a conventional KBr pellet press (International Crystal Laboratories) with ~70 mg of powder. Pellet dimensions were reproducible with this method: 7 mm diameter and ~0.5–0.6 mm thickness (measured using a digital micrometer).

Impedance device architecture

To make a device for impedance analysis, a $MAPbI_3$ pellet was sandwiched between two ion-selective electrodes in a staggered conformation so that some of the ITO-coated portions of each substrate were accessible for clips during sample measurements. This configuration was compressed by clipping the sample with two $\frac{3}{4}$ inch mini spring clamps. A picture of a real device can be found in Fig. S2 (ESI†).

Methylation of poly(4-vinylpyridine)

To a 50 mL round-bottom flask, poly(4-vinylpyridine) (~50 000 kDa, 2.5 g), iodomethane (1.41 mL, 22 mmol), and distilled water (20 mL) were added. The reaction mixture was sonicated for 1 h or until solids had dissolved. The dark yellow solution was concentrated and precipitated in acetone to yield a yellow powder (1.48 g). The product was verified by IR, where the characteristic quaternary ammonium absorptions were observed at 1639 cm^{-1} and 1187 cm^{-1} (Fig. S3, ESI†). For clear impedance results, the product was not dried before testing to allow small amounts of water to act as a plasticizer, boosting ion transport. The impedance response of the product after drying under vacuum overnight showed some signs of ion transport; however,

the resistance was much higher in the dry sample, which led to results with significant noise making it difficult to analyze.

Mass spectrometry samples

Membrane devices were prepared as described above using 40 μL of DEHP. The device was biased at ~1.5 V for 12 h using a standard AA battery attached to each ITO substrate *via* electrical leads. At the conclusion of the experiment, the HOIP sample was removed from the membranes. The surface of the membranes was rinsed with DMF until it ran clear (~0.5 mL). The membranes were then dissolved in DCM, which was subsequently evaporated *via* a gentle stream of air at 60 °C. The membrane powder was sonicated in 0.5 mL millipore water for 2 h. The water solution was filtered through a 0.2 μm polyethersulfone filter. ESI-MS was conducted on the solution in both positive and negative modes.

Characterization

Impedance spectroscopy was performed as a 2-point measurement using a Solartron Analytical SI 1287 Electrochemical Interface with a 1252A Frequency response analyzer. Samples were kept at rt in ambient atmosphere during measurements. Samples were illuminated using a 100 W incandescent light during measurement. AC conductivity was measured in a through-plane configuration from 300 000 to 0.1 Hz at an AC amplitude of 100 mV. DC bias was applied while holding the bottom electrode as a reference to zero any intrinsic parasitic voltage due to imperfect electrodes. The resulting Nyquist plots were modeled and fitted using the ZView software (Scribner Associates).

Powder X-ray diffraction (XRD) was taken in a Bragg–Brentano configuration using a Rigaku SmartLab SE X-ray diffractometer equipped with a D'tex 250 Ultra ID Si strip detector. Measurements were taken from 2θ = 10° to 40° using a Cu K_α (1.542 Å) X-ray source.

Mass analysis was obtained using a Bruker AmaZon ETD quadrupole ion trap mass spectrometer with an electrospray ionization source. The capillary voltage was held at 4.5 kV, and the samples were directly injected at a flow rate of 4 μL min^{-1}. The acquisition time for each sample was ~2 min.

FTIR experiments were run using Bruker Alpha-P equipped with an attenuated total reflectance (ATR) platinum diamond optic. The spectra were recorded between 4000 and 375 cm^{-1} with a resolution of 4 cm^{-1}.

Elemental mapping of the membranes was carried out using Magellan 400 L XHR-SEM equipped with an Oxford X-MAX 80 mm^2 energy-dispersive X-ray spectrometer. The beam acceleration voltage and current were set to 30 kV and 100 pA, respectively. The spectra were recorded up to 20 keV. Wide sample areas of ~500 μm were analyzed.

C. Results and discussion

Electrochemical impedance spectroscopy

In EIS, we can probe materials with non-linear current (I)–voltage (V) relationships. This technique applies an AC voltage and measures the resulting AC current. The use of a sinusoidal voltage allows us to sweep variable frequencies. Therefore, we can probe the conduction processes that occur on a fast (high-frequency) or slow (low-frequency) timescale. The resulting sinusoidal response can be separated into its real and imaginary components and plotted in a complex plane. In EIS, this representation is called a Nyquist plot (Fig. 1b). The shape of the Nyquist plot gives us insights into the physical processes occurring within the system. The most simple electronic semiconductors appear as a single semi-circle in the Nyquist plot. The appearance of additional features indicates the presence of unique conduction processes. High-frequency data points corresponding to faster-timescale conduction processes are represented on the left-most side of the plot (closest to the origin), while the low-frequency data points corresponding to slower-timescale processes are represented by the data on the right side. With this information, we can model the EIS response to determine the specific values for various physical processes.

Ion-selective membrane conductivity

A schematic of our devices is shown in Fig. 1a. We employed an ion-selective membrane (ISM) containing polyvinyl chloride (PVC) as an electronically insulating material, bis(2-ethylhexyl)-phthalate (DEHP) as a membrane solvent, and dibenzo-18-crown-6 (DB18C6) as a cation-selective ionophore (please see chemical structures in Fig. S4, ESI†). We chose this membrane because of its high selectivity for MA^+ ions and because it displays a near-Nernstian behavior for ions in a solution.[14–17]

First, we measured the impedance response of pristine ISM sandwiched between two ITO-coated substrates (Fig. 2a and b). We saw a response extending into low frequencies, which is a characteristic of an electronically insulating dielectric material and has been observed for plasticized PVC membranes.[18] Due to the thickness of the HOIP pellets (~mm) and the electronically insulating nature of ISM, we expected minimal contribution from electronic charge carriers in the response of the full device. To verify this, we measured the EIS response of a conductive bronze plate sandwiched between two ISM-coated

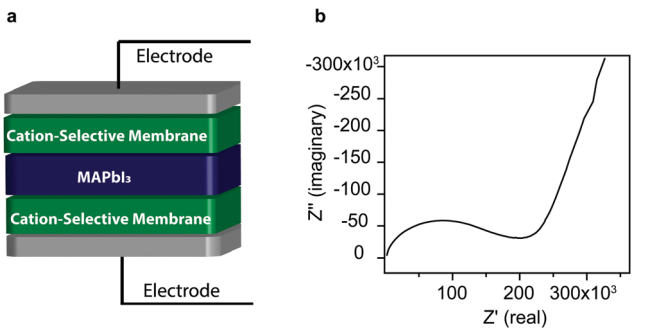

Fig. 1 (a) A device schematic. The electrodes are indium tin oxide (ITO)-coated glass. The ITO substrates were coated with a cation-selective ISM. A pellet of HOIP powder was sandwiched between two ion-selective electrodes, and the device was held together with spring-loaded clamps. (b) The EIS response from the device in (a).

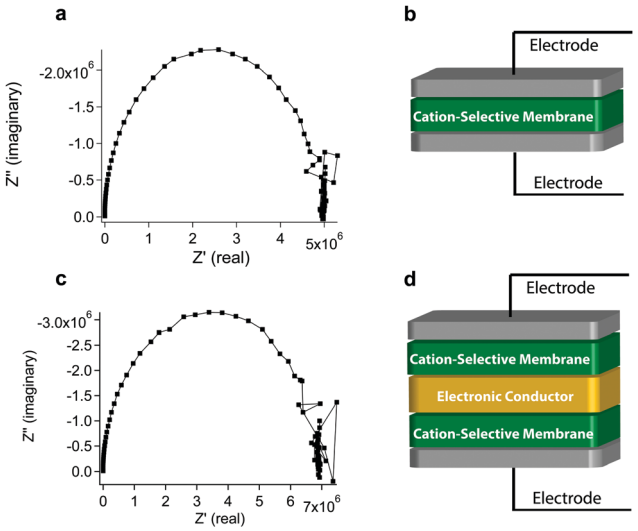

Fig. 2 (a) EIS response of a sample set up as shown in (b). This complex EIS response has been observed before in PVC membranes containing plasticizer and depicts a relaxation of dipoles. (b) A schematic of the device from (a). (c) EIS response of a sample set up as shown in (d). We observe no new features that correspond to electronic conduction through ISM.

electrodes (Fig. 2c and d). We expected to see new features in the high-frequency region of the Nyquist plot if there was a significant electronic contribution. However, the EIS response of the bronze plates sandwiched between the two ISM-coated electrodes was similar to that of pristine ISMs, indicating that there was no electronic contribution from the membranes as expected.

Having established that ISMs are electronically blocking, we then used ISM-coated electrodes to measure the EIS response of a pellet of $MAPbI_3$ under illumination (please see Fig. S5 and S6 (ESI†) for the EIS response of pristine $MAPbI_3$ and the ISM device under dark conditions). The EIS response of this device is shown as a Nyquist plot in Fig. 1b. We observed new features in the Nyquist plot, which were absent in the EIS responses of pristine ISM and bronze plate-ISM controls. As the ISMs are electronically blocking, we attributed this new response to ionic conductivity within the HOIP sample. We also considered an alternate possibility that this response might arise from the MA^+ ions adsorbed onto ISM at the ISM–HOIP interface. We therefore examined the EIS responses of the pellets of methylammonium iodide (MAI) and lead iodide (PbI_2) sandwiched between ISM electrodes. Both these materials are poor ionic conductors. In both samples, there were no EIS responses, which were consistent with poor ionic conductivity. Based on these results, we discounted the possibility that the adsorbed MA^+ ion at the ISM–HOIP interface was the cause of the EIS response we observed in our ISM devices.

ISM chemical characterization

Having established that a selective ionic response was observed in the EIS of our ISM–HOIP devices, we then characterized ISM to establish the chemical identity of the mobile ion. Since we chose ISM to be selective for MA^+, we expected to see the chemical signatures of MA^+ in ISM after experimentation. To test this, we sandwiched a HOIP pellet between two ISM-coated electrodes and applied a bias of 1.5 V under illumination for 12 h. We carefully peeled the HOIP pellet from ISM. The chemical analysis of the resulting membranes with Fourier transform infrared (FTIR) spectroscopy showed evidence of MA^+ incorporated into ISM characterized by absorption peaks between 1500–1600 cm^{-1} and 1490 cm^{-1} attributed to the N–H and C–H bending vibrations, respectively (Fig. S7, ESI†).[19] However, we note that the pristine ionophore DB18C6 also absorbs in this region and hence, this result is not conclusive for MA^+. We then conducted an identical experiment but after peeling away the HOIP pellet, we rinsed the surface of ISM with dimethylformamide (DMF) to remove any excess HOIP materials stuck to ISM after experimentation. We analyzed the chemical composition of the remaining membrane material in the solution using ESI-MS (Fig. 3). We observed the characteristic peak corresponding to DB18C6 complexed to MA^+ at 392.2 m/z, which was consistent with the monoisotopic mass and isotopic distribution of this species. We additionally observed DB18C6 complexes with Na^+ and K^+ at 383.2 and 399.2, respectively. DB18C6 readily complexes with both Na^+ and K^+. Thus, these peaks were anticipated and likely represented ambient impurity during the experimental workup.

We did not observe the characteristic peaks associated with Pb^{2+} or I^- (in the negative ion mode) of free ions or ions complexed to DB18C6 in the ESI-MS spectra (Fig. 4). Since the binding constant ($\log k_a$) values for ammonium cations and Pb^{2+} are similar with respect to DB18C6 (2.94 and 5.05,

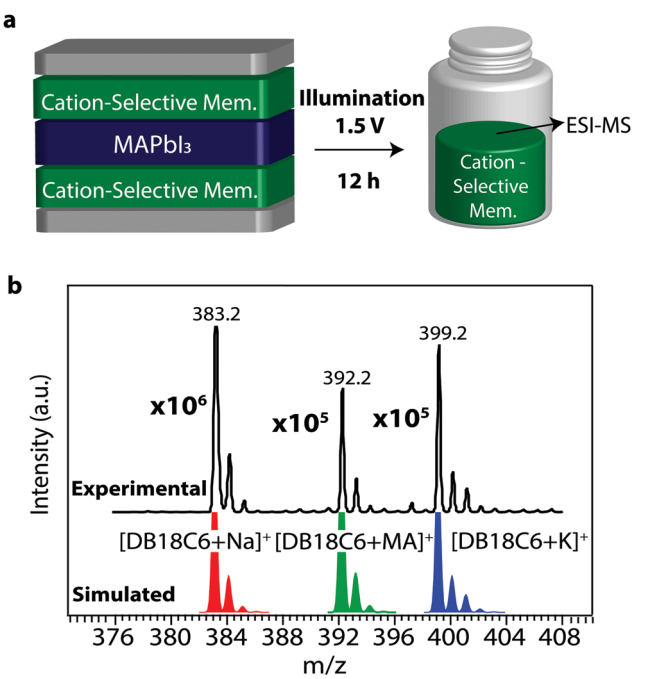

Fig. 3 (a) Schematic of ESI-MS experimental conditions. (b) ESI-MS spectrum obtained in the positive mode of the membranes after the experiment. Peaks are observed corresponding to DB18C6 complexed to MA^+, Na^+, and K^+, as illustrated by the simulated spectra for these charged complexes.

respectively, measured by polarography),[20] simple diffusion of MA^+ into the membrane cannot account for the appearance of this species since we would expect similar diffusion of Pb^{2+} ions. This observation also confirmed that the observed MA^+ peak is not from the excess HOIP sample stuck on the membranes after the DMF washing step. Energy-dispersive X-ray (EDX) analysis of the membranes after exposure to the HOIP sample showed EDX peaks at energy values associated with iodine that is barely discernible from the baseline noise (Fig. S8, ESI†). Thus, we conclude that I^- may be present in ISM at concentrations equal to or below the detection limit of the instrument (1000 ppm), which does not represent a significant contribution when compared to MA^+.

We note that the purpose of these experiments was to impose harsh conditions on the sample for an extended period of time to determine which ions (if any) diffuse within the HOIP and into the membranes. This is not to say that the timescale by which these characterization measurements were conducted (h) is comparable to the timescale on which ion transport is observed in HOIPs (ms). Given the fact that MA^+ was the only ion that was observed in ISMs, it is reasonable to conclude that if Pb^{2+}, H^+ or I^- is mobile in HOIPs, then, ISM would present a blocking boundary for these ions, which should result in particular EIS features. In order to determine the EIS response of our ISMs given known anionic and cationic conduction, we conducted control experiments using (1) a positive control of poly(styrene sulfonate)sodium salt (PSS), where the anionic polymer backbone facilitates Na^+ conduction, and (2) a negative control of poly(*N*-methyl-4-vinylpyridinium iodide) (PVPI), where the cationic polymer backbone facilitates I^- conduction (for structures, please see Fig. S3 and S10, ESI†).

The EIS spectra of pristine PSS and PVPI show features attributable to ionic conduction (Fig. S9 and S10, ESI†). Since our ISM is a cation-selective membrane, we expected the PSS–ISM interface to be a cation-adsorbing interface and the PVPI–ISM interface to be an anion-blocking interface. The influence of these interfacial characteristics on mass diffusion impedance is well documented and can be qualitatively assessed based on the low-frequency response.[13] Warburg mass diffusion typically manifests as a linear 45° region on the Nyquist plot, followed by either a curvature back into the real axis in the case of an absorbing boundary or up to a vertical capacitive line in the case of a blocking boundary.[21] In the case of PVPI, we saw a response characteristic of blocking consistent with the cationic selectivity of ISM (Fig. S9, ESI†). In the positive control containing mobile Na^+, we did not observe the same blocking response (Fig. S10, ESI†). Interestingly, in the positive control, we did not observe a defined 45° linear region characteristic of Warburg ion diffusion. In the case of Warburg mass diffusion, a significant depression of the linear angle (as low as almost 0°) has been reported for systems in the case of absorbing boundary conditions and in systems where the diffusion of conducting particles is complicated by a primary ion adsorption process.[13] It is noteworthy that for the HOIP sample under illumination, we observed a response strikingly similar to that of our Na^+ conductive control, which indicated that the observed EIS response for our HOIP sample arises from mobile cations. However, we cannot conclusively rule out the presence of I^- below the detection limits of ESI-MS and EDX in these membranes. We therefore conclude that MA^+ is the primary ionic species within ISMs during device measurements, and we speculate that this ion is (at least in part) responsible for the observed EIS response.

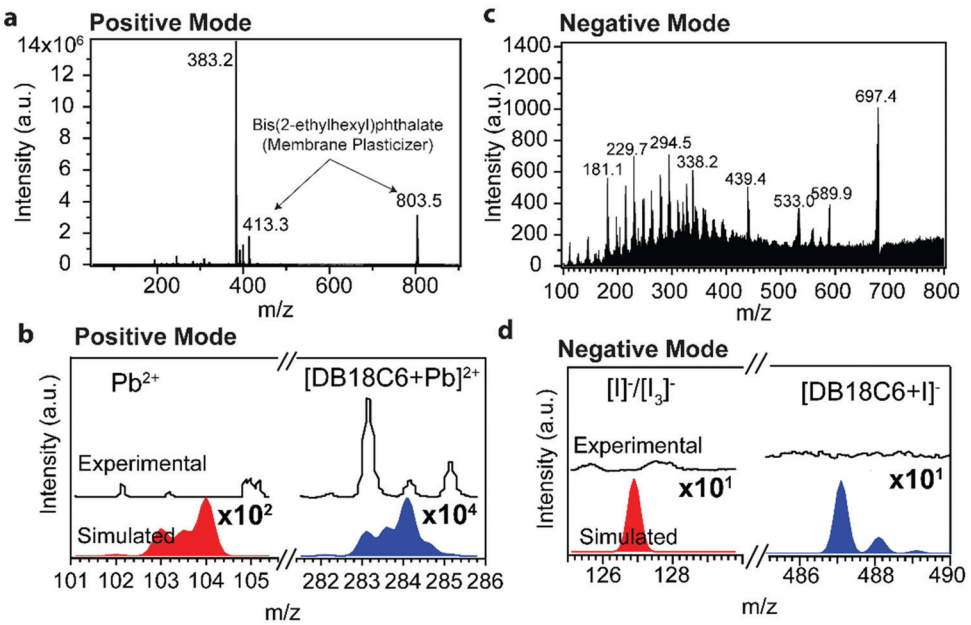

Fig. 4 (a) Mass spectrum taken in the positive mode of the membrane solution after the experiment from Fig. 2a was run. (b) Zoomed in from (a) shows experimental (top) and simulated (bottom) spectra from the anticipated region of either bound or unbound Pb^{2+}. (c) Mass spectrum taken in the negative mode of the membrane solution after experiment. (d) Zoomed in from (c) shows experimental (top) and simulated (bottom) spectra from the anticipated region of either bound or unbound I^-.

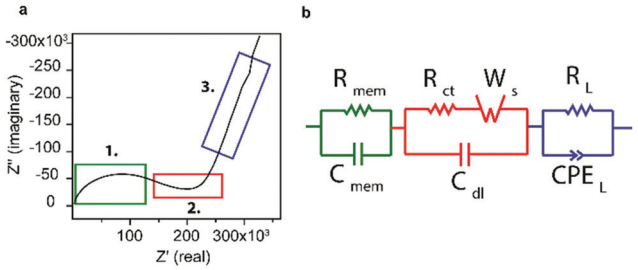

Fig. 5 (a) The EIS response of the ISM device separated into high-frequency (1.) mid-frequency (2.) and low-frequency (3.) response. (b) The proposed circuit model representing the EIS response. The high-frequency response is fitted to an *R*–*C* circuit arising from membrane bulk capacitance, the mid-frequency region is fitted with a Warburg element to capture ion diffusion, and the low-frequency response is fitted to another *R*–*C* modeling leaky capacitance arising from electronic or ionic accumulation.

Modeling the EIS response

The impedance response of the HOIP samples sandwiched between ISM electrodes can be broken into three distinct sections: (1) a high-frequency semicircle, (2) a mid-frequency depressed linear region and (3) a low-frequency capacitive response (Fig. 5). To model this response, we turned to the literature detailing EIS modeling of supercapacitor devices, where ions are incorporated into porous electrodes. We reasoned that these systems are similar to our devices. Therefore, we used a commonly utilized supercapacitor model[22–24] as a scaffold to design our equivalent circuit (Fig. S11, ESI†). This model consists of a Warburg component, modeling ion diffusion to an absorbing boundary in the high- to mid-frequency region, and a resistor and a capacitor (or constant phase element) in parallel (*R*-CPE) in the low-frequency region to model the resistance and capacitance associated with leakage of the capacitor. Ion diffusion is always associated with charge transfer resistance (R_{ct}) and double-layer capacitance (C_{dl}). This literature model provided reasonable fits to our experimental data; however, the fits deviated in the high- and mid-frequency regions. Thus, to model our data, we expanded the circuit to include an additional *R*–*C* component in the high-frequency range to account for the bulk resistance and capacitance of ISM. We reasoned that ISM resulted in non-negligible impedance; therefore, it should be represented in our model. The resulting equivalent circuit is shown in Fig. 5b. This model provides good fits to the data, as measured by the low sum of squares and χ^2 values (Fig. S11, ESI†). We also considered the possibility that the low-frequency component may arise due to ion diffusion to a blocking boundary, which would be the case for MA^+ diffusion to the ITO interface or I^- diffusion to the ISM interface. To test this, we modeled the system with no low-frequency *R*-CPE and instead modified the model with an open Warburg element to reflect blocking boundary conditions (Fig. S11, ESI†). However, this modified model did not fit the data as closely as the model from Fig. 5b; thus, we assume that the low-frequency component is due to ion diffusion to an absorbing boundary. This is consistent with MA^+ diffusion to ISM.

When we fit our data to the model in Fig. 5b, the Warburg element modeling ion diffusion fits to a time constant of the order of ms (~10 ms), which is similar to what has been observed for mobile ions in thin-film photovoltaic devices. Considering the dimensions of the pellet and taking into account the Warburg diffusion resistance, we estimate the ionic conductivity of the mobile ion to be of the order of 10^{-7}–10^{-8} S cm^{-1}, which is also in the range of what we have observed for ions in thin-film devices.[7]

It is important to point out that there remains a significant debate regarding the nature of the mobile ion(s) in HOIP photovoltaics, specifically with regard to the timescale of MA^+ and I^- migration. It has been established that I^- is likely mobile under device-operating conditions.[25–27] However, there is less consensus on the timescale of migration for this ion. Some reports speculate that ultrafast I^- migration occurs on the sub-μs timescale (<1 μs),[8] while others report I^- migration on a slow-μs to fast-ms timescale.[28,29] For studies that have reported the migration of MA^+, the timescale for migration is even more contested; timescales ranging from ms[8,30] to s[31,32] to ~1000 s[33] have been reported. In this work, we observed a response that was consistent with cation migration, which fitted to a ms time constant. We noted that the data presented in this work were consistent with those of MA^+. However, seeing that I^- conduction may also occur on the ms timescale, there is a possibility that this ion contributes to the EIS response of our system. At this point, we cannot comment on the contribution of anionic species since our ISMs were selective only to cations. A full validation of this model including the use of anionic selective membranes is the scope of our future work.

Importantly, the results from the $MAPbI_3$ pellets with ISMs were consistent with the observations for thin-film photovoltaic devices without ISMs. This is a promising result, which demonstrates that this technique can be applied to selectively study ion migration in HOIP devices using EIS. We are currently in the process of placing ISMs on thin-film photovoltaic devices to study ion transport under device-operating conditions and validating the equivalent circuit model through other experiments. We will report the results of these investigations in due course.

D. Conclusions

We showed that placing cation-selective ISMs between the sample and electrodes allows us to measure ion-selective EIS. We deployed this system to study ionic diffusion in HOIPs under illumination. With this device, we showed evidence of impedance arising from ionic conduction through the HOIP material. We proved that ISMs are selective for MA^+, confirming the mobility of this cation. Furthermore, the EIS response in our system could fit to a ms time constant, which suggested that MA^+ may be mobile on this timescale.

Conflicts of interest

There are no conflicts to declare.

Acknowledgements

We gratefully acknowledge the financial support of Army Natick Soldier R D and E Center through contract no. W911QY1820002 for this work. The acquisition of the powder X-ray diffractometer was made possible through the National Science Foundation Major Research Instrumentation Program (CHE-1726578). We also thank Prof. Richard Vachet for his help with mass spectrometry. We gratefully acknowledge the helpful and insightful comments from the reviewers.

Notes and references

1 W. Tress, N. Marinova, T. Moehl, S. M. Zakeeruddin, M. K. Nazeeruddin and M. Gratzel, *Energy Environ. Sci.*, 2015, **8**, 995–1004.
2 S. Meloni, T. Moehl, W. Tress, M. Franckevicius, M. Saliba, Y. H. Lee, P. Gao, M. K. Nazeeruddin, S. M. Zakeeruddin, U. Rothlisberger and M. Graetzel, *Nat. Commun.*, 2016, **7**, 9.
3 G. Richardson, S. E. J. O'Kane, R. G. Niemann, T. A. Peltola, J. M. Foster, P. J. Cameron and A. B. Walker, *Energy Environ. Sci.*, 2016, **9**, 1476–1485.
4 I. Levine, P. K. Nayak, J. T. W. Wang, N. Sakai, S. Van Reenen, T. M. Brenner, S. Mukhopadhyay, H. J. Snaith, G. Hodes and D. Cahen, *J. Phys. Chem. C*, 2016, **120**, 16399–16411.
5 S. van Reenen, M. Kemerink and H. J. Snaith, *J. Phys. Chem. Lett.*, 2015, **6**, 3808–3814.
6 C. Eames, J. M. Frost, P. R. F. Barnes, B. C. O'Regan, A. Walsh and M. S. Islam, *Nat. Commun.*, 2015, **6**, 8.
7 J. Haruyama, K. Sodeyama, L. Y. Han and Y. Tateyama, *J. Am. Chem. Soc.*, 2015, **137**, 10048–10051.
8 J. M. Azpiroz, E. Mosconi, J. Bisquert and F. De Angelis, *Energy Environ. Sci.*, 2015, **8**, 2118–2127.
9 A. Pockett, G. E. Eperon, N. Sakai, H. J. Snaith, L. M. Peter and P. J. Cameron, *Phys. Chem. Chem. Phys.*, 2017, **19**, 5959–5970.
10 M. N. F. Hoque, N. Islam, Z. Li, G. F. Ren, K. Zhu and Z. Y. Fan, *ChemSusChem*, 2016, **9**, 2692–2698.
11 E. C. Smith, C. L. C. Ellis, H. Javaid, L. A. Renna, Y. Liu, T. P. Russell, M. Bag and D. Venkataraman, *J. Phys. Chem. C*, 2018, **122**, 13986–13994.
12 D. Pitarch-Tena, T. T. Ngo, M. Valles-Pelarda, T. Pauporte and I. Mora-Sero, *ACS Energy Lett.*, 2018, **3**, 1044–1048.
13 V. F. Lvovich, *Impedance Spectroscopy: Applications to Electrochemical and Dielectric Phenomena*, John Wiley & Sons, Inc., Hoboken, New Jersey, 2012.
14 T. Katsu and M. Matsumoto, *Anal. Sci.*, 2001, **17**, 721–725.
15 T. Katsu and N. Nishimura, *Anal. Sci.*, 2000, **16**, 523–525.
16 T. Katsu, D. F. Xu, K. Tsuji and T. Nagamatsu, *Anal. Chim. Acta*, 1997, **354**, 301–305.
17 M. A. Akl and M. H. Abd El-Aziz, *Arabian J. Chem.*, 2016, **9**, S878–S888.
18 M. O'Rourke, N. Duffy, R. D. Marco and I. Potter, *Membranes*, 2011, **1**, 132–148.
19 M. S. Yin, F. X. Xie, H. Chen, X. D. Yang, F. Ye, E. B. Bi, Y. Z. Wu, M. T. Cai and L. Y. Han, *J. Mater. Chem. A*, 2016, **4**, 8548–8553.
20 R. M. Izatt, K. Pawlak, J. S. Bradshaw and R. L. Bruening, *Chem. Rev.*, 1991, **91**, 1721–2085.
21 J. Landesfeind, D. Pritzl and H. A. Gasteiger, *J. Electrochem. Soc.*, 2017, **164**, A1773–A1783.
22 W. Wang, S. R. Guo, I. Lee, K. Ahmed, J. B. Zhong, Z. Favors, F. Zaera, M. Ozkan and C. S. Ozkan, *Sci. Rep.*, 2014, **4**, 9.
23 C. Masarapu, H. F. Zeng, K. H. Hung and B. Q. Wei, *ACS Nano*, 2009, **3**, 2199–2206.
24 R. S. Hastak, P. Sivaraman, D. D. Potphode, K. Shashidhara and A. B. Samui, *Electrochim. Acta*, 2012, **59**, 296–303.
25 D. W. Dequilettes, W. Zhang, V. M. Burlakov, D. J. Graham, T. Leijtens, A. Osherov, V. Bulovic, H. J. Snaith, D. S. Ginger and S. D. Stranks, *Nat. Commun.*, 2016, **7**, 9.
26 A. Senocrate, I. Moudrakovski, G. Y. Kim, T. Y. Yang, G. Gregori, M. Gratzel and J. Maier, *Angew. Chem., Int. Ed.*, 2017, **56**, 7755–7759.
27 T. Y. Yang, G. Gregori, N. Pellet, M. Gratzel and J. Maier, *Angew. Chem., Int. Ed.*, 2015, **54**, 7905–7910.
28 S. A. L. Weber, I. M. Hermes, S. H. Turren-Cruz, C. Gort, V. W. Bergmann, L. Gilson, A. Hagfeldt, M. Graetzel, W. Tress and R. Berger, *Energy Environ. Sci.*, 2018, **11**, 2404–2413.
29 C. Li, A. Guerrero, S. Huettner and J. Bisquert, *Nat. Commun.*, 2018, **9**, 8.
30 M. Bag, L. A. Renna, R. Y. Adhikari, S. Karak, F. Liu, P. M. Lahti, T. P. Russell, M. T. Tuominen and D. Venkataraman, *J. Am. Chem. Soc.*, 2015, **137**, 13130–13137.
31 Y. B. Yuan, J. Chae, Y. C. Shao, Q. Wang, Z. G. Xiao, A. Centrone and J. S. Huang, *Adv. Energy Mater.*, 2015, **5**, 7.
32 M. H. Futscher, J. M. Lee, L. McGovern, L. A. Muscarella, T. Wang, M. I. Haider, A. Fakharuddin, L. Schmidt-Mende and B. Ehrler, *Mater. Horiz.*, 2019, **6**, 1497–1503.
33 K. Domanski, B. Roose, T. Matsui, M. Saliba, S. H. Turren-Cruz, J. P. Correa-Baena, C. Roldan-Carmona, G. Richardson, J. M. Foster, F. De Angelis, J. M. Ball, A. Petrozza, N. Mine, M. K. Nazeeruddin, W. Tress, M. Gratzel, U. Steiner, A. Hagfeldt and A. Abate, *Energy Environ. Sci.*, 2017, **10**, 604–613.

